Downloaded from orbit.dtu.dk on: Apr 19, 2025

DTU Library

Numerical prediction of the galling of aluminium alloys in cold strip drawing

Filali, Oussama; Dubois, André; Moghadam, Marcel; Nielsen, Chris V.; Dubar, Laurent

Published in:
Journal of Manufacturing Processes

Link to article, DOI:
10.1016/j.jmapro.2021.11.008

Publication date:
2022

Document Version
Peer reviewed version

Link back to DTU Orbit

Citation (APA):
Filali, O., Dubois, A., Moghadam, M., Nielsen, C. V., & Dubar, L. (2022). Numerical prediction of the galling of aluminium alloys in cold strip drawing. *Journal of Manufacturing Processes*, *73*, 340-353. https://doi.org/10.1016/j.jmapro.2021.11.008

General rights
Copyright and moral rights for the publications made accessible in the public portal are retained by the authors and/or other copyright owners and it is a condition of accessing publications that users recognise and abide by the legal requirements associated with these rights.

- Users may download and print one copy of any publication from the public portal for the purpose of private study or research.
- You may not further distribute the material or use it for any profit-making activity or commercial gain
- You may freely distribute the URL identifying the publication in the public portal

If you believe that this document breaches copyright please contact us providing details, and we will remove access to the work immediately and investigate your claim.

Numerical prediction of the galling of aluminium alloys in cold strip drawing

Oussama FILALI[a], André DUBOIS[a*], Marcel MOGHADAM[b], Chris V. NIELSEN[b], and Laurent DUBAR[a]

[a]Université Polytechnique Hauts de France, LAMIH - CNRS UMR 8201, Institut Carnot ARTS, INSA Hauts de France, F-59313 Valenciennes, France
[b]Department of Mechanical Engineering, Technical University of Denmark, Kongens Lyngby, Denmark

Corresponding author:

Pr. André Dubois
Laboratoire d'Automatique, de Mécanique et d'Informatique indistrielles et Humaines (LAMIH), UMR CNRS 8201

Université Polytechnique Hauts de France,

Le Mont Houy,

59313, Valenciennes Cedex

email : andre.dubois@uphf.fr

Abstract

A methodology based on finite element computations is proposed to predict the galling onset of aluminium alloys in cold forming. The methodology assumes that galling starts as soon as a finite element in the area of contact has reached a critical damage. The damage is calculated using Xue's model, which takes into account the effect of tangential stresses on the damage evolution. The tangential stress is calculated using Wilson's mixed lubrication model taking into account the roughness of the tools. Strip reduction tests were performed on aluminium AA6082 specimens, with and without lubricant. The proposed numerical model is in good agreement with experiments and is able to predict the onset of galling. The model is sufficiently accurate to determine the effect of tool roughness.

Keywords:

Aluminium alloy, galling onset, mixed lubrication, finite element model, damage model, Lode angle

1 - Introduction

Environmental issues have promoted the use of aluminium alloys (AA) and high strength steels (HSS) in the automotive and aerospace industries. Their physical and mechanical properties make them advantageous for the design of lighter vehicles, which contributes to the reduction of the carbon footprint [TUR20]. Compared to carbon steel, the lightweight property of HSS comes from their high yield stress. HSS components can support the same load with smaller cross-sectional area than equivalent carbon steel components. Regarding aluminium alloys, their lightweight property comes from the low density of aluminium [SHE16], while alloying elements facilitate a high level of yield stress. Even if their physical and mechanical properties are totally different, both HSS and AA materials share the same manufacturing issue: they are prone to galling by pick-up on forming tools and subsequent scoring [BIL12][BAY97][DAN06]. The galling propensity of aluminium and aluminium alloys is due to the brittle nature of the oxide layer. Deformation will cause the oxide layer to break up and expose virgin metal, which is very prone to pick-up on the tool surface in case of insufficient lubrication [BAY 94]. Galling tendencies of HSS components are often attributed to their high yield stress, because HSS components require high contact pressure to be formed, and this leads to increased tool/workpiece interface temperature and lubricant film breakdown that initiates galling [COR09][AND98].

According to ASTM, galling is a form of surface damage arising between sliding solids; it is “a severe form of adhesive wear characterized by the formation of excrescences – macroscopic protuberances generated by adhesion between the rubbing surfaces” [BUD97]. This definition by the ASTM appears incomplete for metal forming applications. Galling can be formulated as a lubrication film breakdown resulting in pick-up of workpiece material to the tool surface, which results in scoring of subsequent workpiece material. Galling has been widely studied in the fields of cold and hot metal forming, stamping and machining. These studies are mainly based on experiments and back in 1999, P.J. Blau and K.C. Budinski already counted almost twenty ASTM standard wear tests among which at least a quarter could be used to study the galling phenomenon [BLA99]. Many other friction tests are also commonly used to study galling, such as the two crossed cylinders test [HAN08], the U-bending test [SCH94], the deep drawing test [KIM07] or the strip reduction test [AND98]. Each of these tests simulates different tribological conditions in terms of contact pressure, plastic strain, sliding velocities and temperature, thereby emulating various conditions of contact encountered in industrial forming or machining processes.

Presented as a strictly qualitative method, the ASTM G98 standard however reports a threshold galling stress used as a ranking value to screen materials [AST98]. This threshold stress is sometimes advanced to explain the tendencies of HSS to gall. Nonetheless, Siefert and Babu report that the determination of the threshold galling stress is not a trivial manner, and may not be applicable for all materials [SIE14]. Hummel [HUM08] reported the same conclusions. Based on the use of a new test designed to operate with a constant contact pressure, Hummel highlights that the propensity for galling does not go through a step transition from non-galled to galled. The notion of a threshold galling stress appears then to be a misnomer.

On the other hand, roughness is known to have a major impact on galling onset. In a recent study, Zabala et al. have tested the effect of strip surface texturing and tool surface polishing on the prevention of galling [ZAB21]. One of their conclusions is that minimum electrical discharge

texturing (EDT) on the aluminium strip is required to avoid galling, while the die surface topography is the dominant factor controlling galling in forming. On rough tool surfaces galling takes place in the vicinity of the grinding scratches: relatively thick deposits are frequently observed in the scratches or in front of the scratches, whatever the materials and the testing method used [HAN09][FIL18] [JER15]. This is characterized by a layer-by-layer material transfer mechanism in the early stages of galling. In addition to the commonly used surface roughness parameters such as the arithmetic mean height Ra or the maximum height Rz, the ratio of peaks to valleys Rpk/Rvk of the tool surface, the peak material volume Vmp, the pit void volume Vvv, and the reduced summit height Spk, are identified to significantly influence the galling kinetics on unlubricated sliding surfaces [KLU16][ZAB21].

However, galling occurs also on smooth tool surfaces [HEI09]. Klünsner et al. [KLU16] explain that in the absence of lubricants and macroscopic surface scratches, galling starts by nucleation of microscopic workpiece material adhesions at microscopic surface asperities. Material transfer on fine polished tool steel surfaces, i.e. with roughness of some nanometres, is dependent on the distribution, size and composition of hard phase particles of the tool steel grades investigated but no chemical surface properties have been clearly identified to promote galling. Results tend to prove that galling is mainly affected by the local geometry and not by the chemistry of the surfaces in contact [HEI13][KAR14][WES16].

Other parameters are also known to influence galling: material plasticity [BUD15], interface temperature [PUJ13][OLS04][TRO17], lubricants and coatings [HEI10][POD17].

All these experimental works are of great help to understand the mechanisms of galling and to develop solutions in order to avoid or to limit this surface defect. The results, however, barely provide information able to predict if galling will occur or not during a forming process. Considering that the cost of the dies in metal forming is up to 30% of the total production costs [DEB16][HAW16], and that galling reduces tool life considerably, developing methods to predict galling becomes a necessity. Yoshikawa et al. [SOE13][WAN14] have developed a prediction method of galling behaviour dedicated to press forming. Based on experimental observations they assume that galling occurs in the area where the temperature is maximum and the material is sliding out of the dies. They use FEM to calculate the temperature field and then predict the galling area. Olsson et al. proposed a prediction method for lubricated contact based on the assumption that the lubricant film breaks down when it reaches a critical temperature determined experimentally [OLS04]. In this model, galling starts as soon as the lubricant film thickness is diminished to the maximum tool roughness causing direct metal-to-metal contact.

Dong et al. have proposed a numerical approach of galling prediction based on the Archard's wear model [DON16]. The model is implemented in a FE software and is used to compute wear depth along the die surface. If the area with the highest wear depth may correspond to galling, the results may be subject to discussion since the predicted wear depth have a magnitude of 10^{-4} mm, which is smaller than the roughness of the dies. Deng et al. [DEN19] used a modified version of Archard's wear model to predict galling. In their model, the specific wear rate is not constant but a function of contact pressure and temperature. The galling simulation precisely predicted the position of severe galling in the tool radius. Moghadam et al. [MOG20] also predicted the location of wear in stamping dies with drawbeads based on Archard's model, taking normal pressure and sliding length into account. The above mentioned methods provide information on the risk of even slight galling to occur using finite element computations of the

full-scale process. The main drawbacks of these methods are that they need an accurate determination of the wear rates of the materials and they do not explicitly take into account the tool roughness.

The present work proposes a new approach to predict galling. Galling is characterised by the presence of adhesive wear, and material has then to be torn from the softer surface to adhere to the harder surface. The tearing of the softer material can be seen as the first step of galling. The methodologies commonly used to study ductile failure can be applied to detect the galling onset. In this work, the onset of galling is assumed to occur when the material in the vicinity of the contact area reaches a critical damage, Dc, before being torn off the surface. The damage to be compared with Dc is computed with a damage model that takes into account the effect of shear stresses, since the surfaces are subjected to friction stresses. The friction model applied in the finite element computations explicitly takes into account the surface roughness. In the present work, the methodology is applied to the Strip Reduction Test developed at DTU [UST17].

2 – The damage model

Many phenomenological and micromechanical damage models have been developed to study ductile failure. Phenomenological models are based on continuum damage mechanics (CDM). Popularised by Lemaitre [LEM85], these models involve a damage variable coupled into constitutive equations representing the continuous deterioration of elastic stiffness and material strength. Damage measurements are convenient and require the identification of a few parameters [LEM12]. The damage increment is related to the equivalent plastic strain increment and the damage strain energy release rate, which facilitates the description of the stress triaxiality effect on damage parameters [LEM85, YU19]. Many extended damage-coupled yield criteria derive from this model [BON05, BRU18, MAL14, NGU15, SAA94]. On the other hand, micromechanical models predict the evolution of void volume within the material by modelling the nucleation, growth, and coalescence of initial voids present in the material volume. These models are based on the Gurson's model [GUR77] and they have been widely used to predict the evolution of damage in metal forming and other applications [GAO09, GOL93, LAU97, TVE84, XUE07].

A first study had been carried out to investigate the capability of Lemaitre and Gurson-Tvergaard-Needleman (GTN) damage models to predict the galling onset [PHA15]. Galling experiments were performed on AA 6082 specimens using the Upsetting-Sliding Test (UST) [DUB96]. Finite element models of the UST were used to simulate the experiments, where galling occurred. A first model adopted a macroscopic approach. The vicinity of the surfaces was modelled with quadratic elements of 0.1 mm x 0.1 mm and the surface of the tool was assumed smooth. A second model adopted a mesoscopic approach. The vicinity of the surfaces was modelled with quadratic elements of 0.033 mm x 0.033 mm and the roughness of the tool was modelled. Both FE models were run with Lemaitre's and with GTN damage models. Neither of the damage models involved showed critical damage in the contact area with the macroscopic models. Critical damage was observed only in some computations performed with the mesoscopic model and Lemaitre's damage model. These results were explained by the fact that the contact area was mainly subjected to compressive and shear stresses, while classical damage models are only sensitive to tensile stresses. The roughness in the mesoscopic model modified the stress state near the surface, such that tensile stresses occurred between the asperities [BEL08], leading to damage. Nevertheless, these tensile stresses were large enough to generate a

critical damage only in the most extreme conditions of contact. These FE models were then considered not accurate enough to predict galling onset [DUB17].

To overcome this issue computations have to consider the effect of shear stresses on damage evolution. The damage model developed by Xue is used in the present work [XUE07]. This damage model has been successfully applied to study various metal forming processes [CAO15, MAL12, ZEH19]. In this model, the shear stresses are considered by the Lode parameter. The damage model is governed by the following equations [XUE09]:

$$\sigma_{eq} = (1 - D^{\beta})\sigma_M(\varepsilon_p) \tag{1}$$

$$\dot{D} = m\left(\frac{\varepsilon_p}{\varepsilon_f}\right)^{m-1}\frac{\dot{\varepsilon_p}}{\varepsilon_f} \tag{2}$$

$$\varepsilon_f = \varepsilon_{f0}\mu_p(p)\mu_\theta(\overline{\theta}) = \varepsilon_{f0}\left[1 - qlog\left(1 - \frac{p}{p_{lim}}\right)\right]\left[\gamma + (1-\gamma)\left|\overline{\theta}\right|^k\right] \tag{3}$$

where σ_{eq} is the equivalent stress, σ_M is the equivalent matrix stress, ε_p is the current plastic strain, D is the damage parameter, $\dot{D}$ is the damage rate, ε_f is the fracture envelope, p is the hydrostatic pressure and $\overline{\theta}$ is the Lode parameter given by:

$$\overline{\theta} = -\frac{6}{\pi}\tan^{-1}\left(\frac{1}{\sqrt{3}}\frac{2\sigma_{II} - \sigma_I - \sigma_{III}}{\sigma_I - \sigma_{III}}\right) \tag{4}$$

where σ_I, σ_{II} and σ_{III} are the ordered principal stress components. The equivalent stress is calculated using the Bai-Wierzbicki general form of asymmetric metal plasticity [BAI08]. According to Cao's work, the correction term in pressure is neglected [CAO13]. Equation (1) is then rewritten as:

$$\sigma_{eq} = (1 - D^{\beta})\left[C_s + (C_{ax} - C_s)\left(\bar{\theta}^2 - \frac{\bar{\theta}^{2k_p}}{2k_p}\right)\right]\hat{\sigma}_M(\varepsilon_p) \tag{5}$$

where $\hat{\sigma}_M(\varepsilon_p)$ is the intrinsic stress–strain property and C_s, C_{ax}, k_p are material parameters. The damage to fracture transition takes place when the damage parameter D reaches the critical value Dc. Therefore, the Xue's damage model requires the identification of 11 material parameters: the damage exponent m, the weakening exponent β, the reference fracture strain ε_{f0}, the shape parameter q, the limiting pressure p_{lim}, the fracture strain ratio γ, the critical damage Dc, the Lode angle dependence exponent k, and the Lode angle correction parameters C_s, C_{ax}, k_p.

The damage model is implemented in Abaqus. The kill element option is used to remove elements where critical damage Dc is reached.

3 – The friction model

The reliability of the numerical prediction of galling depends on the knowledge of the stress state in the vicinity of the contact area. The contact pressure is quite independent of the tribological conditions [GUE99, DUB96]. Nonetheless, the prediction of the friction stress is more complex and requires friction laws able to model the complexity of the chemical, physical and mechanical interactions at the tool/workpiece interface [KIH90]. The main friction models used in metal forming are the constant friction model, the second generation models based on the crushing of asperities and the third generation models based on fluid-structure interaction to consider explicitly the effect of liquid lubrication on friction [DUB16, NIE18, YAN08]. The friction models used in the present work derive from Wilson's work on mixed and boundary lubrication in metal forming [WIL88, WIL90, WIL91]. One of the advantages of these models is their ability to take into account the tool roughness as an input parameter. The computation of the friction stress operates in three steps [WIL95]. The first step is the appraisal of the normalized film thickness z. The second step is the identification of the lubrication regime. The third step is the calculation of the friction stress. The lubricant normalized film thickness *z* is given by:

$$\mathrm{z} = \frac{h}{3R_{eq}} = \frac{h}{3\sqrt{R_{qW}^2 + R_{qT}^2}} \tag{6}$$

where h is the film thickness and R_{qW} and R_{qT} are the quadratic mean roughness of the workpiece and of the tool, respectively. In the present work the calculation of thickness h derives from the Hamrock and Dowson's equations in which correction factors are introduced to take into account the thermal changes between the bath and the inlet zone and the shear-thinning effects in the contact zone [Bair07, ECH17]:

$$h = \varphi_t h_{Nc} \varphi_{st} \tag{7}$$

where h_{Nc} is the Newtonian central film thickness at bath temperature, φ_t is the thermal correction factor and φ_{st} is the shear thinning correction factor:

$$h_{Nc} = 1.55\alpha^{0.53}(\eta_0 v_m)^{0.67} E'^{0.06} R^{0,33} \overline{p}^{-0.2} \tag{8}$$

$$\varphi_t = \frac{1 - 13.2\left(\frac{\overline{p}}{E'}\right) L_t^{0.42}}{1 + 0.213\left[1 + 2.23\left(\frac{v_s}{v_m}\right)^{0.83}\right] L_t^{0.64}} \; with \; L_t = \frac{\beta \eta_0 v_m^2}{K_l} \tag{9}$$

$$\varphi_{st} = \left[1 + 0.79\left(\left(1 + \frac{v_s}{v_m}\right)\frac{v_m \eta_0}{\varphi_t h_{Nc} G}\right)^{\frac{v_m}{v_m + 0.2 v_s}}\right]^{-3.6(1-n)^{1.7}} \tag{10}$$

In these equations, $\overline{p}$ is the mean contact pressure, R is the contact radius, α is the pressure-viscosity coefficient, β is the temperature-viscosity coefficient, E' is the tool-workpiece reduced Young's modulus, G is the lubricant shear modulus, v_s is the relative sliding speed, v_m is the average contact speed, η_0 is the viscosity at room temperature, K_l is the lubricant thermal conductivity, and n is an exponent dependent on the lubricant [ECH11].

When z is larger than 3, the contact is in the thick film regime. The friction stress results from shearing of the lubricant. Its expression is a function of the viscosity of the lubricant η_G, the relative sliding speed v_s and lubricant film thickness h:

$$\tau_{thickfilm} = \eta_G \frac{v_s}{h} \tag{11}$$

In the present study, the Carreau's equation is applied to take into account the effect of the hydrostatic pressure p_E and the shear rate $\dot{\gamma}$ on the viscosity of the lubricant:

$$\eta_G = \eta_0 e^{\alpha p_E} \left[1 + \left(\frac{\eta_0 e^{\alpha p_E} \dot{\gamma}}{G}\right)^2\right]^{\frac{n-1}{2}} \tag{12}$$

where η_0 is the viscosity at ambient pressure.

When z is ranging from 1 to 3, the contact is in the thin film regime. A shear stress factor is then introduced to take into account the effect of the roughness on the lubricant flow [PAT78]:

$$\tau_{thinfilm} = \phi_{thinfilm} \eta_G \frac{v_s}{h} \tag{13}$$

$$\begin{aligned} \phi_{thinfilm} &= 4.81z^2 - 5.83z^4 + 2.19z^6 \\ &+ (1.09z - 3.28z^3 + 3.28z^5 - 1.08z^7) \ln\left(\frac{z+1}{z-1}\right) \end{aligned} \tag{14}$$

When z is lower than one, direct contact between the tool and workpiece surfaces occurs. The lubrication regime is mixed if a liquid lubricant is used, or boundary if a solid lubricant or no lubricant is used. In the mixed lubrication regime, the friction stress is given by:

$$\tau_{mixed} = (\tau_a + \tau_p)A + \phi_{mixed} \eta_G \frac{v_s}{h}(1 - A) \tag{15}$$

where A is the fractional area of contact, τ_a is the adhesive friction stress and τ_p is the ploughing friction stresses, both occurring at the asperity level. Assuming a rough tool sliding on a smooth workpiece, these mechanical quantities are given by [WIL88, WIL91, WIL98]:

$$\tau_a = m_0 k \tag{16}$$

$$\tau_p = \frac{\overline{p} tan\theta}{A} = p_a tan\theta \tag{17}$$

$$A = 0.5 - 1.09z + 1.09z^3 - 0.66z^5 + 0.16z^7 \tag{18}$$

$$\begin{aligned}\phi_{mixed} = {} & 5.24z + 2.41z^2 - 12.43z^3 - 2.92z^4 + 17.99z^5 + 1.09z^6 - 3.56z^7 \\ & + (1.09z - 3.28z^3 + 3.28z^5 - 1.08z^7)\ln(z+1)\end{aligned} \tag{19}$$

where m_0 is the adhesion coefficient, which is equivalent to the friction factor at the microscopic scale, p is the mean contact pressure, p_a is the microscopic contact pressure, k is the shear yield stress and θ is the mean slope of tool asperities (Fig. 1).

In the boundary lubrication regime, the fractional area of contact A is obtained by assuming a partial contact along the asperities (Fig. 1b). Under this assumption, A is lower or equal to 0.5 and is identified from the following equation [WIL91]:

$$\frac{2k}{\overline{p}} = (-0.86A^2 + 0.345A + 0.515)\frac{\bar{d}_{II} l(1-A)}{v_s tan\theta} + \frac{1}{(2.571 - A - \mathrm{Aln}(1-A))} \tag{20}$$

where $\bar{d}_{II}$ is the strain rate in the vicinity of the contact surface and $2l$ is the distance between two asperities. The friction stress is given by:

$$\tau_{boundary-partial} = Am_0 k + \overline{p} tan\theta \tag{21}$$

If equation (20) leads to a fractional area A larger than 0.5, the assumption of partial contact is incorrect, and the contact is then complete (Fig. 1c) and A equals 1. In this condition, the ploughing stress depends on the pressure on both sides of the asperities and cannot be calculated from the mean pressure $\overline{p}$ alone. The friction stress is then given by [WIL88, WIL91, KOR92]:

$$\tau_{boundary-complete} = m_0 k + \frac{2v_s tan^2\theta}{0.472\bar{d}_{II} l + 0.828 v_s tan\theta} k \tag{22}$$

These friction models are implemented in ABAQUS with the VFRICTION user subroutine. The input data of the subroutine are the coefficient of adhesion m_0, the slope and the distance of tool asperities θ and $2l$ and the lubricant properties. The output is the friction stress.

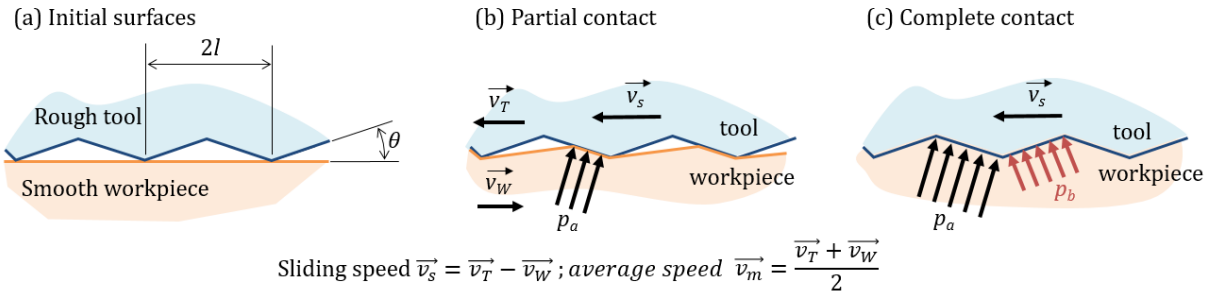

Sliding speed $\overrightarrow{v_s} = \overrightarrow{v_T} - \overrightarrow{v_W}$; *average speed* $\overrightarrow{v_m} = \frac{\overrightarrow{v_T} + \overrightarrow{v_W}}{2}$

Figure 1. Micro contact geometry of the Wilson friction model [WIL91].

4 – The material

The aluminium alloy AA6082-T4 is considered in this research. This material is commonly used for car body and chassis parts in the automobile industry [ROD14]. Table 1 provides the chemical composition of the material.

Table 1: Chemical composition of AA 6082 (% by mass)

Si	Fe	Cu	Mn	Mg	Cr	Ni	Zn	Al
0.92	0.41	0.07	0.58	0.78	0.04	0.01	0.03	Bal.

Tensile and shear tests were performed to identify the material parameters. Specimens were machined from a 2 mm thick cold rolled plate according to the geometries given in Fig. 2. Tensile tests achieved in the longitudinal and transversal directions of the plate revealed no anisotropic behaviour of the material [PRU17]. Shear tests were performed with stereo Digital Image Correlation (DIC) technique to map the strain in surface.

According to Cao et al. and Xue, the value for k, m, q and Cs for aluminium alloys can be chosen as $k = 1$, $m = 2$, $q = 1.5$, $C_s = 1$ [XUE07, CAO13, CAO14]. The fracture strain ratio γ is defined as the shear effective strains over the tensile effective strains at failure. So it is identified directly from tests results. The remaining parameters are obtained from inverse identification applied to the beginning of the tensile force-displacement curves first, to the shear force-displacement curves second, and to the end of the tensile force-displacement curves last. The beginning of the tensile curves provide the intrinsic stress-strain curve (assuming no damage occurs for small plastic strain). Then the shear test curves lead to the identification of the Lode angle correction parameters C_{ax} and k_p. Finally the end of the tensile curves allows the identification of damage parameters Dc, p_{lim}, β and ε_{f0} (Fig. 3). The stress-strain curve is given by equation (23) and material and damage parameters are given in Table 2. All of these parameters are validated by comparing the FE results of the shear test to the experimental data coming from the stereo DIC and not used in the identification procedure. A good agreement is obtained in terms of final shape, localisation and range of equivalent plastic strain (Fig. 4).

$$\hat{\sigma}_M(\varepsilon_p) = 205\left(1 + 90.9\,\varepsilon_p\right)^{0.21}\ MPa \qquad (23)$$

Table 2: material and damage parameters for the 6082-T4 aluminium alloy

ε_{f0}	Dc	m	k	p_{lim}	q	γ	β	Cs	Cax	kp
1,25	0,34	2	1	800	1,5	1,2	1	1	0.89	6

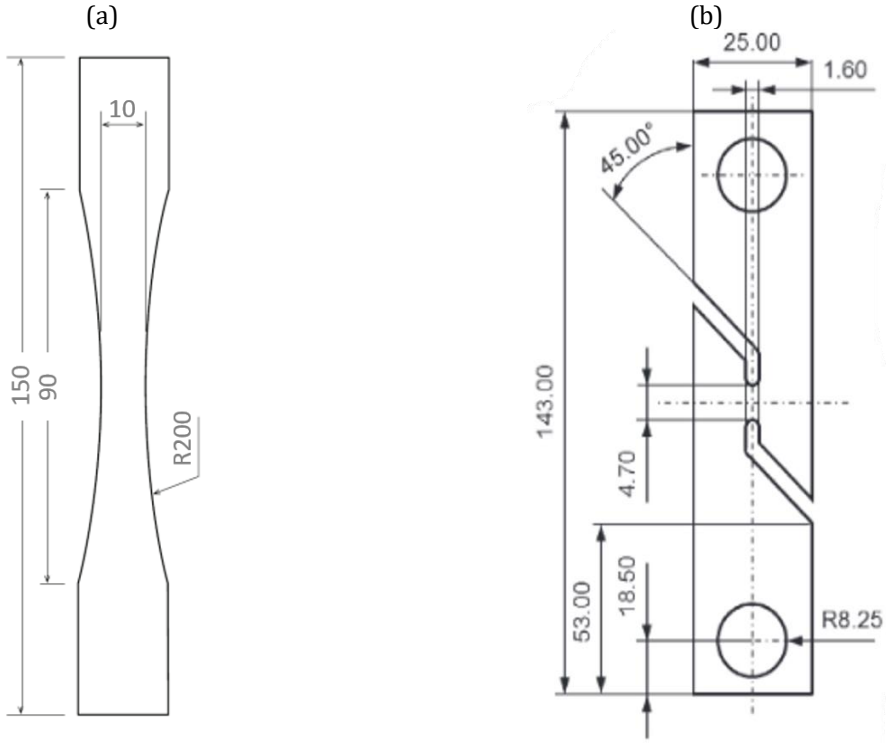

Figure 2. (a) Tensile specimen, from [HUB11], (b) shear specimen, from [MER13]

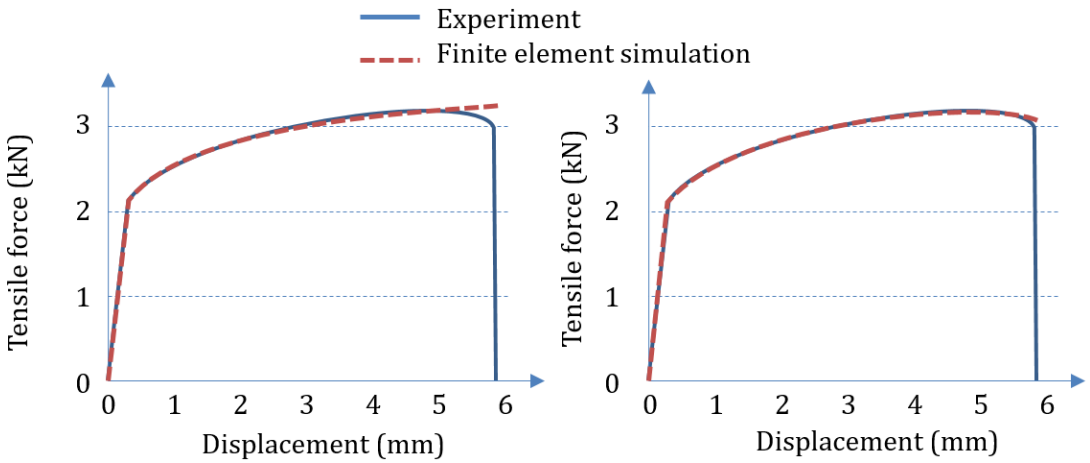

Figure 3. Numerical vs experimental tensile forces. (a) Computation performed after the identification of the intrinsic stress-strain curve (without damage) (b) Computation performed after the identification of the damage parameters.

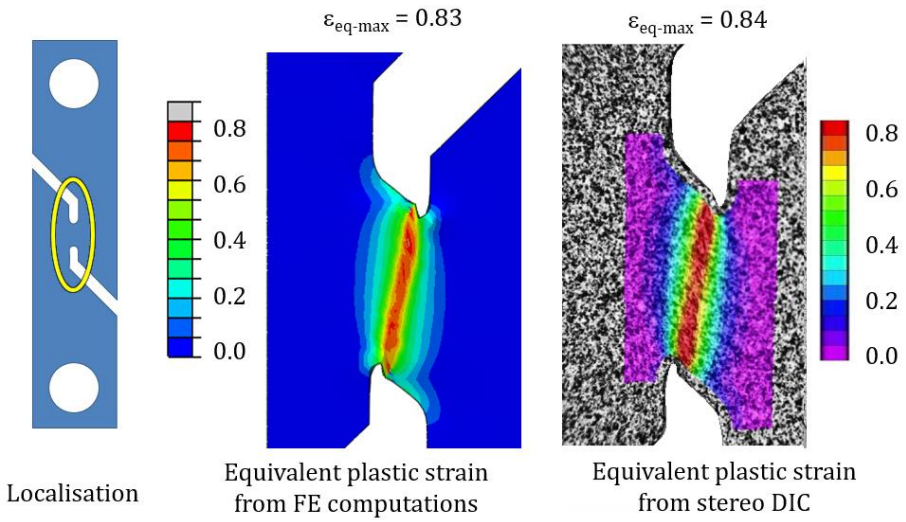

Figure 4. Validation of the damage model. Experimental vs numerical equivalent plastic strain just before rupture.

5 - Galling experiments

5-1 Design of experiments

Galling experiments were performed by the Strip Reduction Test (SRT). Initially designed to study the ironing process, the SRT has been used with success to study the limits of lubrication, and the galling onset occurring in metal forming [AND98, OLS04, UST17].

The SRT involves a strip that is pulled through two fixed tools in order to reduce its thickness. Tools may be two flat dies, a circular cylindric pin and a flat die or two circular cylindric pins. The cylindric pin tools do not rotate and their spacing is adjusted by the use of gauge blocks (Fig. 5). Main test inputs are the percent of strip reduction, the sliding length, the strip exit speed, the temperature of strip and tools, strip and tools roughness and the properties of the lubricant when the tests are lubricated. The sliding length can be adjusted to multiple short distances to get closer to production conditions, as proposed by Üstünyagiz et al. [UST17, UST18, UST19], or set to a long sliding distance for fundamental study of accumulated lubrication and wear mechanisms. Main test outputs are drawing force F_T recorded during the tests and the sliding distance before the first scratch occurs on the strip *Ls*, as defined in [LAZ98]. Acoustic emission may be used to detect the galling onset and the tools roughness can be measured after the tests to quantify the severity of the galling [MOG17, DUB18]. The clamping force F_C required to obtain a specific reduction ratio is unknown and cannot be used to identify a coefficient of friction.

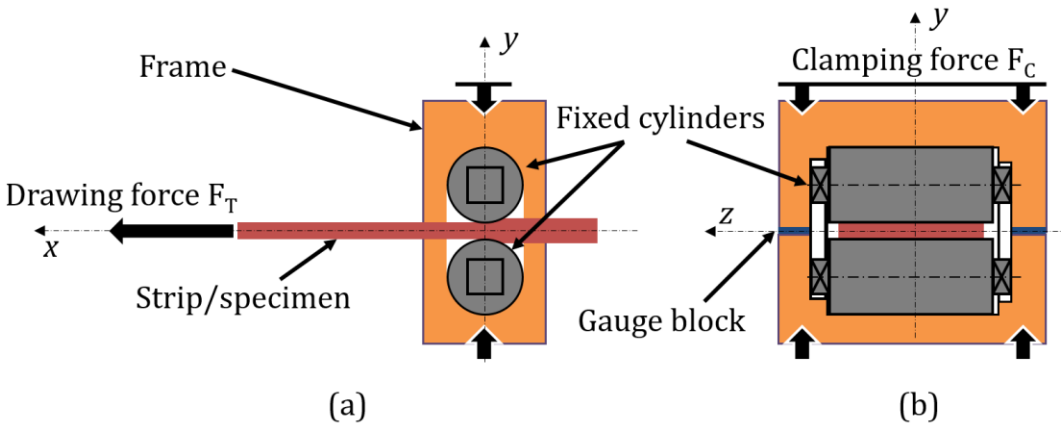

Figure 5. SRT sketch. (a) cross-section view, (b) front view.

The design of experiments is shown in Table 3. The initial dimensions of the specimens were a total length of 500 mm, a width of 30 mm and a thickness of 1 mm. Two sets of experiments were performed: set 1 with lubricant and with large thickness reduction, set 2 without lubricant and with small thickness reduction. The drawing speed was set to 100 mm/s and the total sliding length was 300 mm. The SRT tools were AISI H11 steel circular cylindric pins of 15 mm diameter and 35 mm width. The mean arithmetic roughness of the tools were measured prior to the test using the Alicona InfiniteFocus optical surface measurement system.

In the present work, the SRT tools were hand polished. Each tool was prepared on a mini-lathe machine with a rotation speed of 300 rpm and an operator applies a constant pressure on the tool surface using a 500 grit SiC paper. The polishing ridges are thereby in the direction of the drawing. Although they were polished with care, the roughness of the upper and lower tools were different. The arithmetical mean roughness *Ra* and the rms slope *Rdq* are given in Table 4. These testing conditions lead to a mean equivalent plastic strain ranging from 0.08 to 0.19, which is sufficient to generate intermetallic particles removal without affecting the grain size itself [BOU15].

Table 3: Design of experiments.

Test parameter	set 1				set 2				
thickness reduction (%)	16	20	25	30	7	9	10	12	15
lubricant	mineral oil				no lubricant				
drawing speed (mm/s)	100				100				
temperature (°C)	20				20				
total sliding length(mm)	300				300				
reference of tools	F				A	B	C	D	E

Table 4: Experiments, roughness, slope and half distance of asperities on upper (Up) and lower (Lo) tools before the tests

Tool	A		B		C		D		E		F	
reference	*Up*	*Lo*	*Up*	*Lo*	*Up*	*Lo*	*Up*	*Lo*	*Up*	*Lo*	*Up*	*Lo*
Ra (µm)	0.3	0.3	0.3	1.0	0.3	0.5	0.3	0.7	0.9	0.3	0.3	0.4
Rdq (°)	4	4	4	13	4	5	7	4	4	8	4	4
θ (rad)	0.07	0.07	0.07	0.23	0.07	0.09	0.12	0.07	0.07	0.14	0.07	0.07
l (µm)	17.1	17.1	17.1	17.3	17.1	22.8	9.8	40.0	51.5	8.5	17.1	22.9

5-2 Experimental results – Drawing force

For the lubricated tests, the drawing forces are quite steady and follow the same tendency (Fig. 6a). Logically, the higher reduction, the greater drawing force. In the case of the 30% reduction, a sudden rupture of the specimen after a drawing distance of 100 mm was observed. Figure 6b presents the drawing force curves for the unlubricated tests. Three different behaviours are observed. For the reduction of 7%, the variation of drawing force is similar to that of the lubricated tests. For reduction of 10%, the level of the drawing force is close to that obtained at 7% but the curve presents some fluctuations, with a first maximum within the first ten millimetres of drawing, a second maximum after about 130 mm, and finally a continuous increase after 210 mm. Finally, for reductions of 9, 12 and 15%, the drawing force increases and reaches a first maximum around 30-40 mm of drawing, then decreases until a drawing of 50-60 mm, then increases again significantly until the rupture of the strip. The specimen with the highest reduction rate breaks first but no logical correlation between the maximum value of the drawing force and the reduction rate is noticed. This result suggests that the contact conditions are so deteriorated that the friction energy becomes dominant rather than the plastic strain energy.

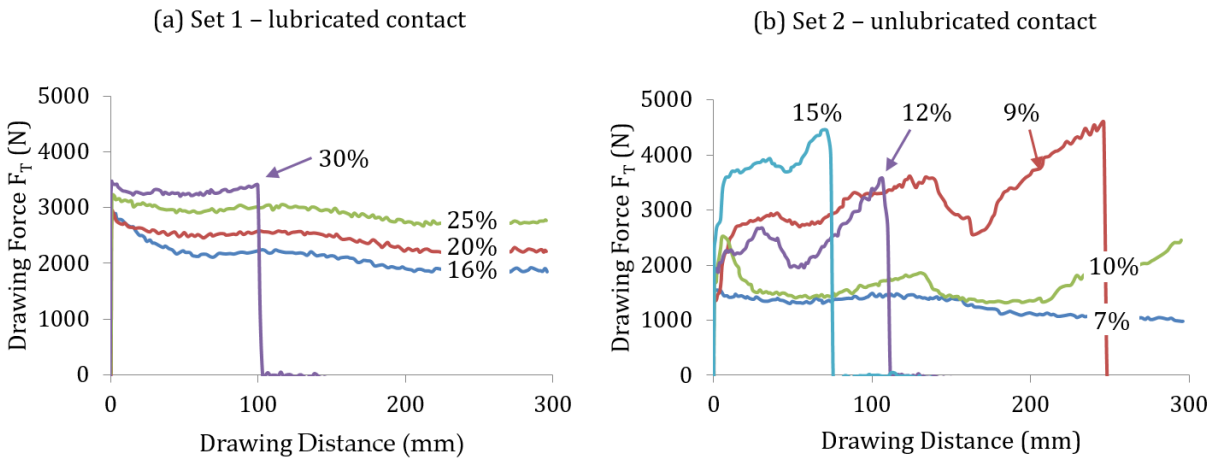

Figure 6: Experimental drawing force vs drawing distance for (a) lubricated and (b) unlubricated contact.

5-3 Experimental results – sliding length before the first scratch Ls

Seizure is characterized by the appearance of an increasingly dense network of scratches, removal of material and, in the most severe cases, the appearance of networks of cracks. In the present study, it is assumed that galling onset occurs as soon as the tearing of the material from the strip is visually observable.

The lubricated test specimens are presented in Fig. 7. The lower and upper surfaces of the specimens showed a few light scratches at the start of the test. With the exception of the 30% case, these scratches tend to fade after a few millimetres of displacement. For the 30% case, the surface present marked scratches but no cracks or micro-tearing are observed. The tool surface present brighter lines but no galling has occurred (Fig. 8-set1). The brighter lines are

characteristic of a light adhesive wear [UST18]. As shown in Fig. 7 related to the 30% reduction configuration, this light adhesive wear takes the form of ridges along the strip surface. These ridges may exist on a long sliding distance without evolving into galling. The light adhesive wear is then not linked to galling onset, i.e. there were no scratches on the specimen surface, no increase of friction force, and no material transfer strongly adherent to the tool surface.

The non-lubricated test specimens are presented in Fig. 9. The visual appearance of the test specimen at 7% is similar to that observed during the lubricated tests. The surface showed only a few scratches at the beginning of the test and no more significant defects afterwards. No pick-up of workpiece material is observed on the tools. For specimens with a reduction of 9, 12 and 15%, significant marks are observed along the strip, which are accentuated before the rupture zone (Fig. 9b). These defects tend to be localised on the edges of the strips. For these three test configurations, the seizure of the specimen occurs after drawing lengths of 9 mm, 32 mm and 15 mm, respectively. The test performed at 10% of thickness reduction exhibits three distinct zones on the lower side of the strip. The first zone appears after a few millimetres of drawing and the second between 80 and 130 mm. These first two zones affect the specimen only over part of its width with a dense network of light scratches. At 200 mm, a new defect zone starts. The galling onsets at 220 mm sliding length with the occurrence of severe scratches and cracks (Fig. 9c). These different areas are directly correlated to the variation in the drawing force shown in Fig. 6b. No defect is noticed on the upper side of the strip. When seizure occurs, it is observed on both sides of the specimen except for the 10% case. However, it does not always appear symmetrically and with the same severity. These galling observations are correlated with the observation of tool surfaces in Fig. 8. Finally, it is interesting to note the build-up of material at the entrance to the contact zone. Experimental results are summarised in Table 5.

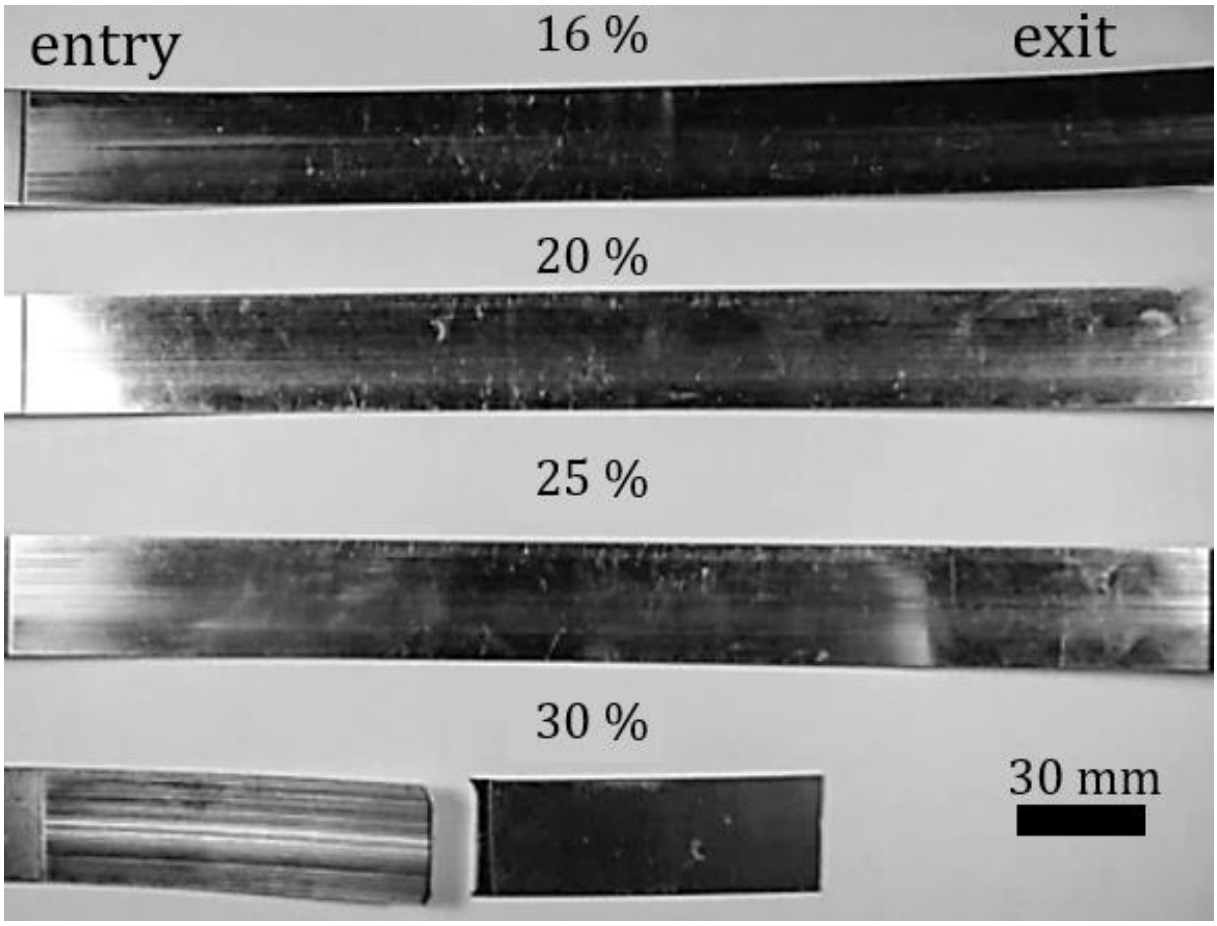

Figure 7: Experiments - set 1. Lubricated tests. Photos of the specimens after testing.

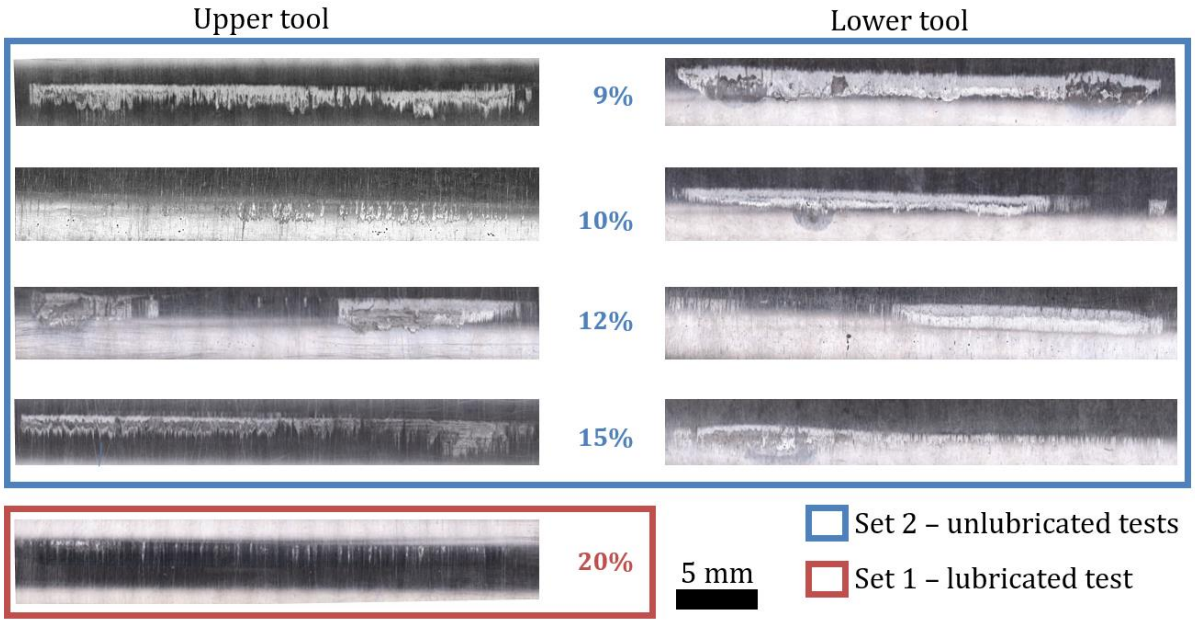

Figure 8: Experiments – set 1 and 2. Photos of the tools after testing.

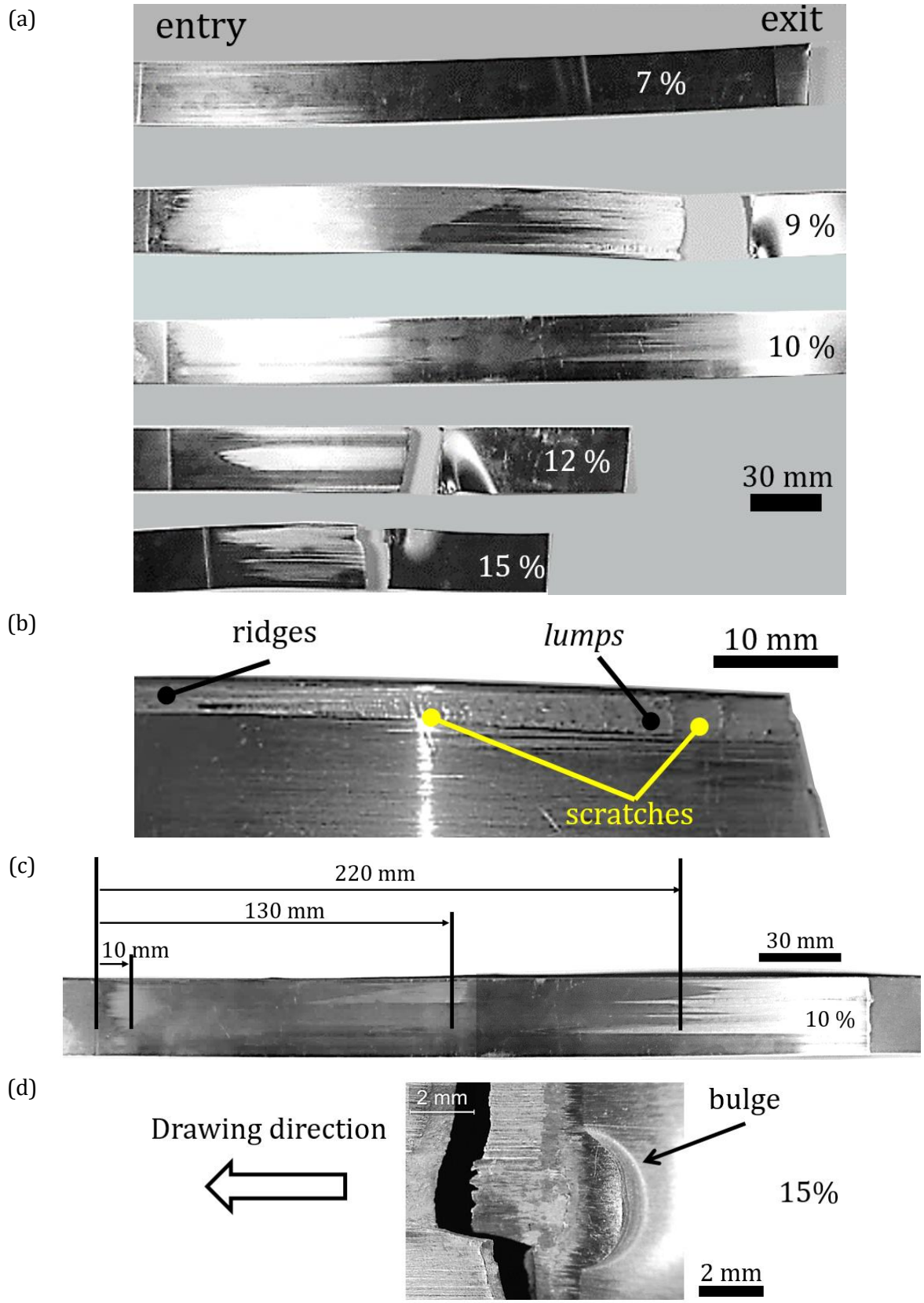

Figure 9: Experiments - set 2. (a) Photos of the specimens after testing; (b) zoom on surface defects in case of 12% of thickness reduction; (c) localisation of the galling area in case of 10% of thickness reduction; (d) zoom on the area of rupture in case of 15% of thickness reduction.

Table 5: Main experimental results.

	set 1				set 2				
Thickness reduction	16	20	25	30	7	9	10	12	15
Ls (mm)	>300	>300	>300	>100	>300	9	220	32	15
galling on upper side	-	-	-	-	-	●	-	●	●
galling on lower side	-	-	-	-	-	●	●	●	●
strip rupture	-	-	-	●	-	●	●	●	●

6 – Prediction of galling prediction by numerical simulations

6-1 Initial mesh and boundary conditions

Computations were performed using ABAQUS Explicit. Xue's damage model and Wilson's lubrication model are implemented using Abaqus user subroutines (Fig. 10). Since the roughness of the upper and lower tools are different, only the symmetry with the xy plane is considered (Fig. 11). This symmetry plane corresponds to z = 0. The mesh of the strip is made of 225,000 thermo-elasto-plastic hexahedral elements with reduced integration C3D8RT of dimensions 0.2 x 0.2 x 0.2 mm^3. The element type and the mesh size are identical to the one used for the inverse identification of the damage models in Section 4. The rheology assigned to the elements is given by equation (23) and the damage parameters in Table 2. Each tool is modelled by 20,720 rigid thermal elements C3D8RT. Their rheology is given by a Young's modulus of 210,000 MPa and a Poisson's ratio of 0.3.

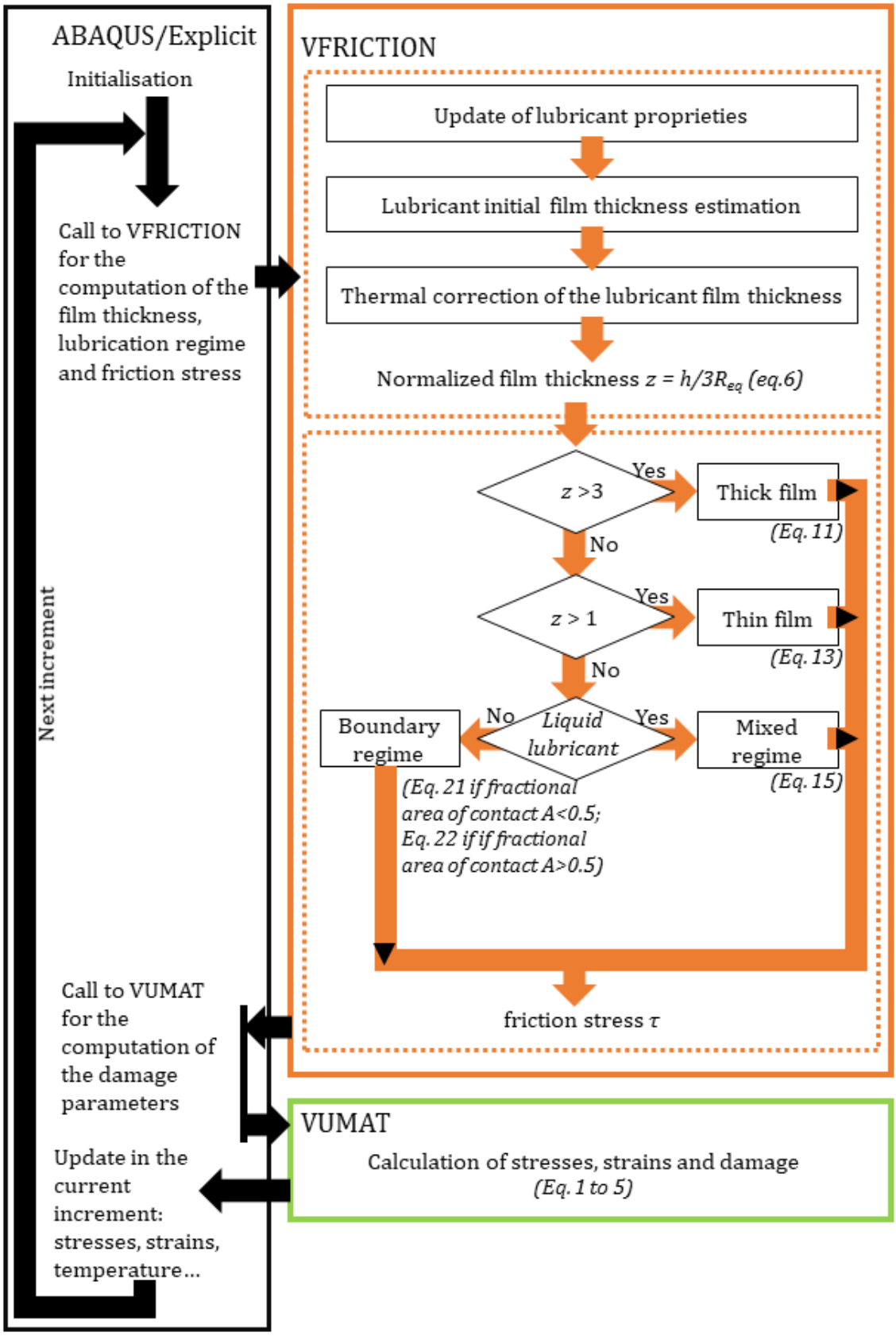

Figure 10: schematic view of the computation algorithm.

The loading operates in two steps. Step 1: the upper and the lower tools move in the y direction to compress the strip. During this step the node set *So* identified in Fig. 11b is blocked. Step 2: the tools are held in position and a displacement of 100 mm or 250 mm in the x direction is imposed on the node set *So*.

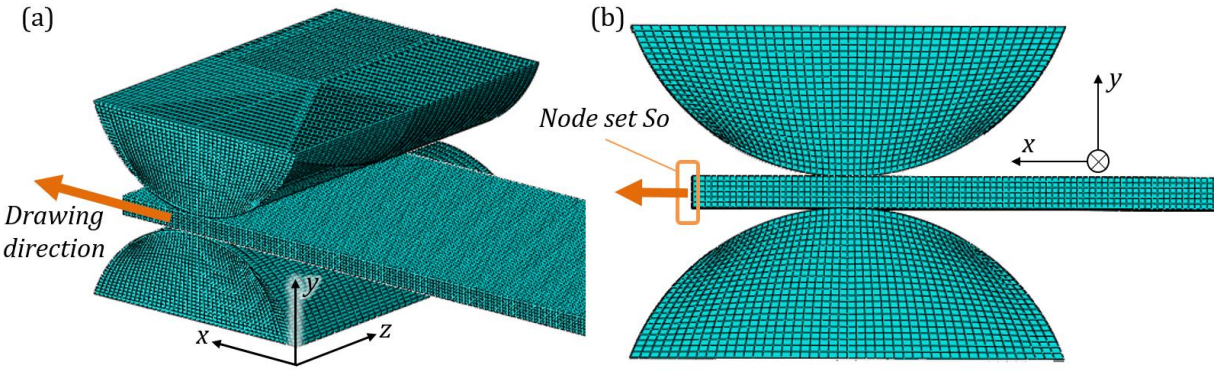

Figure 11: Initial FE mesh of the SRT test shown in (a) perspective and (b) plane view (xy).

6-2 Friction data

According to Section 3, the input data required by the mixed lubrication friction model are the equivalent roughness *Req*, the lubricant properties, the coefficient of adhesion m_0 and the tool asperity slope θ and the distance between tool asperities $2l$. Lubricated tests were performed with a pure mineral oil with properties given in Table 6. The slope and half distance between the tool asperities are given in Table 4. Only the adhesion coefficient m_0 has to be identified. As the compression force F_C is unknown, the coefficients of adhesion are identified by an inverse method by correlating the experimental drawing force with the numerical one. The identification is done for strip displacement in the range of 50 to 100 mm. Two coefficients are identified, m_{01} for the lubricated tests and m_{02} for the unlubricated tests. The identifications are based on the tests performed with the smallest strip reduction, where no galling was observed experimentally. Results are presented in Fig. 12. While the numerical simulations are calibrated by experiments to match the apparent friction, it is noted that the estimated local adhesion is smaller than expected. This might be due to overestimation of the ploughing contribution in the Wilson model. Possible overestimation of ploughing may be attributed to the overall angles determined by profile measurements being larger than the angles associated with rounded, local asperity tips.

Table 6: Physical properties of the mineral oil [ECH17].

viscosity at ambiant pressure η_0	23.4 mPa·s
pressure-viscosity coefficient α	15.7 GPa^{-1}
temperature-viscosity coefficient β	0.033 K^{-1}
lubricant shear modulus G	1 MPa
lubricant thermal conductivity K_l	0.12 W/mK
exponent n	0.5

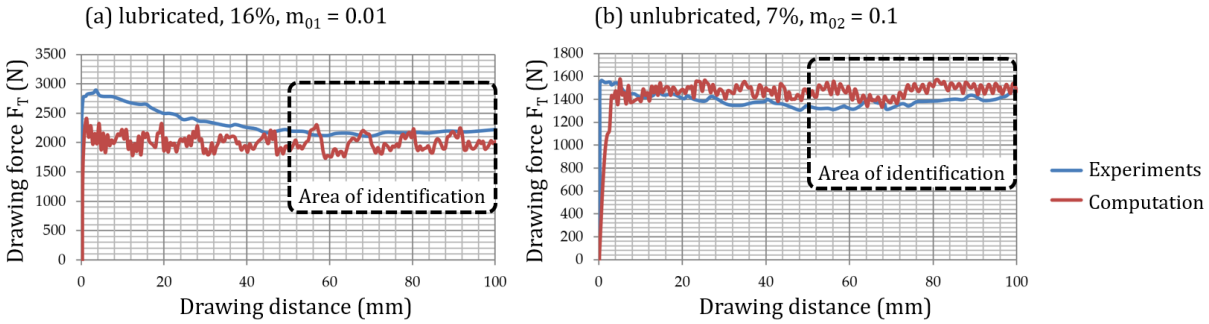

Figure 12: Adhesion coefficients m_0 identified by inverse analysis for (a) set 1of experiments with lubrication and (b) set 2 of experiments without lubrication.

6-3 Finite element results of drawing forces

Fig. 13 presents the evolution of the drawing forces for the lubricated tests. All the computations are carried out with the adhesion coefficient m_{01} = 0.01 identified at 16%. As the tools all have the same roughness, only the thickness reduction is changed from one simulation to another. The numerical results show a good correlation with the experiments. For strip reduction of 30%, the damage model is able to predict the rupture of the strip although it overestimates the drawing distance before rupture (112 mm instead of 100 mm).

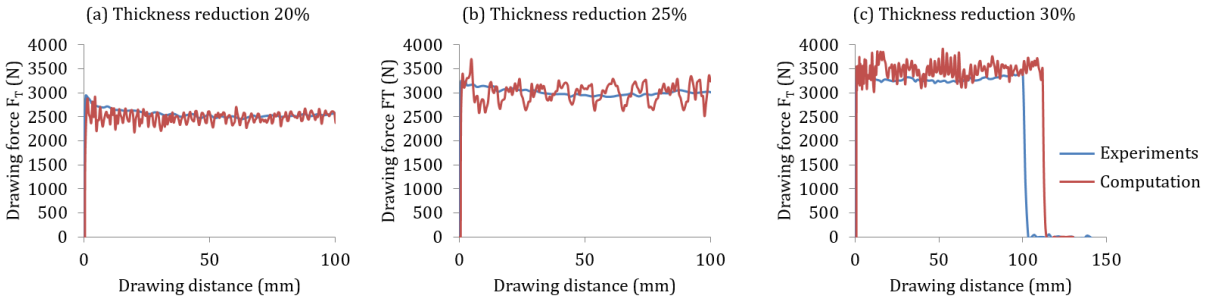

Figure 13: Experimental vs numerical drawing forces for set 1 including lubricated tests at reductions of (a) 20%, (b) 25% and (c) 30%.

Fig. 14 presents the evolution of the drawing forces for the unlubricated tests. Although the computations are run with the same adhesion coefficient m_{02} = 0.1, the friction conditions differ on the two sides of the strips, since the roughness of the lower and upper tools is different. The trends of the drawing forces are very different from the experimental ones. These differences can be explained by the assumptions made in the present work to study the onset of galling. First the fully damaged elements are removed from the strip but they are not transferred to the tool surface. Therefore, as soon as the galling has started, there is a loss of material in the numerical simulation that has no physical meaning. Second, in the experiments, pick-up of workpiece material on the tool surface modifies the tribosystem. The strip no longer comes in contact with steel but with a steel/aluminium layer, which may induce a lower coefficient of friction [HEI09].

The parameters of the friction model, in particular the coefficient of adhesion m_{02} and the roughness parameters l and θ are no longer valid as soon as galling begins and would need to be updated.

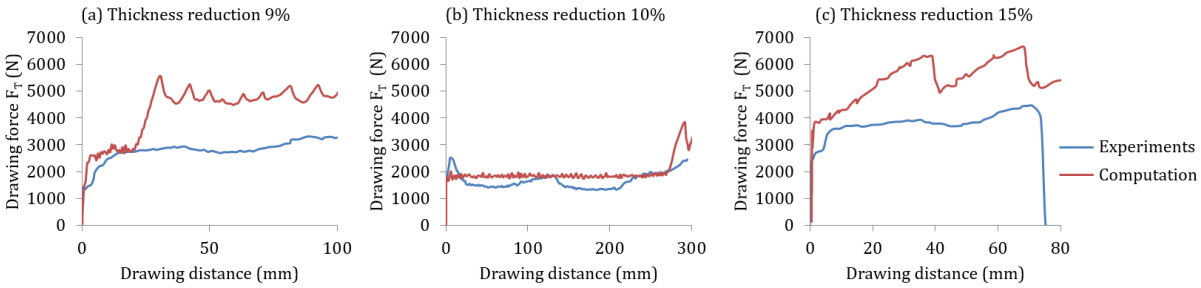

Figure 14: Experimental vs numerical drawing forces for set 2 including unlubricated tests at reductions of (a) 9%, (b) 10% and (c) 15%.

6-4 Prediction of galling onset

In order to identify the onset of galling, this section focusses on three test conditions: lubricated with a high strip reduction (test S1-30%), unlubricated with a small strip reduction (test S2-7%) and unlubricated with a medium strip reduction (test S2-15%). Galling was observed only in the S2-15% configuration.

Fig. 15 presents the contact pressure profiles in the yz plane after 10 mm and 100 mm drawing distances. At these distances, the three configurations present no critical damage. Despite a thickness reduction four times larger, the contact pressure profiles of configurations S1-30% and S2-7% are identical, with a value of 400 MPa over two thirds of the width of the specimen (from z = 0) and a decrease to 220 MPa at the edge. On the other hand, the pressure profile is very different for the S2-15% configuration, with a minimum value on the axis of symmetry (z = 0), a maximum at 500 MPa in z = 8.5 mm, and a decrease at the edge of the strip to reach the same value as cases S1-30% and S2-7% (Fig. 15a). After 100 mm drawing length, the pressure profiles for the S1-30% and the S2-7% configurations remain quite the same as for 10mm, with a slightly lower average value for the S2-7% test (360 MPa). On the other hand the S2-15% configuration presents a strong variation of the contact pressure profile. Its maximum reaches 900 MPa and tends to spread across a 1.5 mm wide area. The contact pressure profiles in the xy plane after a 100 mm drawing distance are given in Fig. 16. Profiles are plotted in the planes z = 0 and z = 7 mm where the contact pressure is maximum. The abscissa x = 0 corresponds to the entrance of the contact area. The increase in reduction naturally leads to an increase in the contact area. For the S2-15% configuration, the increase in the contact length is explained by the material build-up at the entrance to the deformation zone, which significantly increases the thickness of the strip at the entrance. It seems that the amplitude of the contact pressure is more influenced by the friction conditions that generate the material build-up than by the thickness reduction itself. In all cases, the pressure has an absolute maximum at the entrance of the contact and a relative maximum at the output.

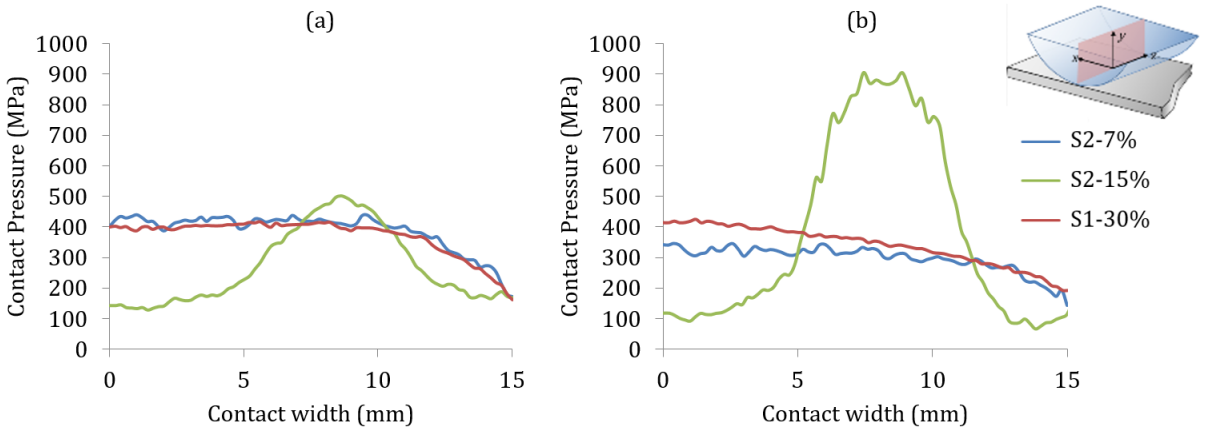

Figure 15: Calculated contact pressure profiles in the yz plane after drawing distances of (a) 10 mm and (b) 100 mm.

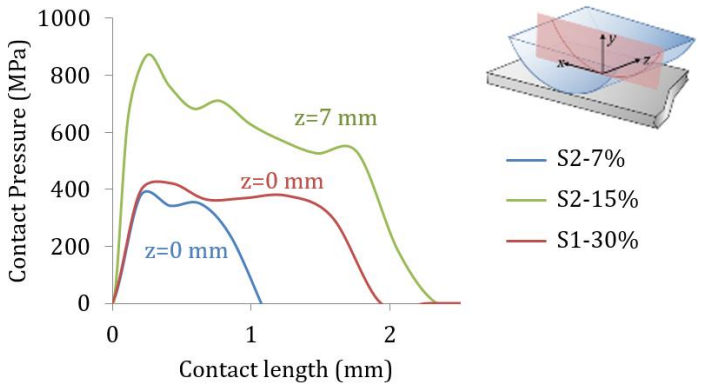

Figure 16: Calculated contact pressure profiles in the xy plane after a drawing distance of 100 mm.

Fig. 17 shows the evolution of the triaxiality η, the Lode parameter $\overline{\theta}$, the damage variable D and the contact pressure after 10 mm of drawing. These values are computed in the strip elements closest to the surface. The curves are drawn in the xy plane, where the contact pressure is maximum (in z = 0 for the S2-7% and S1-30% configurations, and in z = 7 mm for the S1-15% configuration). The damage variable D increases with the strip reduction for all the configurations. The damage at the exit of the contact area is negligible in the case of 7% (around 10^{-3}, equivalent to 0.3% of Dc), moderate in the case of 30% (less than 0.06, 17% of Dc) and strong in the case of 15% (larger than 0.2, 59% of Dc). Evidently, the triaxiality is negative in the contact area, which is mainly in compression, and positive after the exit (mainly in traction). In the S1-30% configuration, where the reduction is high, and in the S2-15% configuration, with unfavourable friction conditions, a compression zone forms at the entrance to the contact area. This leads to a very significant drop in the stress triaxiality η which goes below -1. This compressive zone delays the damage occurrence in the entrance area. Nonetheless, as the strip thickness is reduced and the plastic strain increases, the hydrostatic pressure decreases and the Lode parameter tends to zero. This leads to a decrease of the fracture strain (Eqn. 3) and consequently to an increase of the damage.

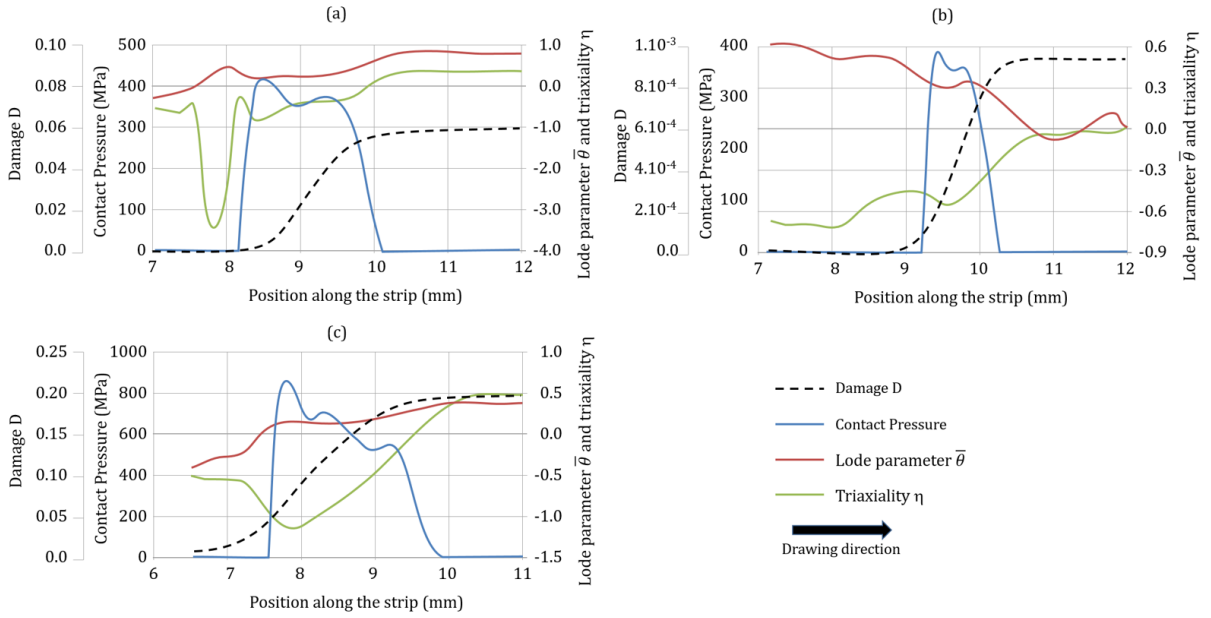

Figure 17: Computations. Calculated damage, Lode parameter and stress triaxiality profiles after a 10 mm drawing distance for the configurations: (a) S1-30%, (b) S2-7% and (c) S2-15%.

The drawing distance before the predicted onset of galling *Ls* is given in Table 7. The numerical value of *Ls* correspond to the drawing distance before the first finite element is delated. No galling is found for the configurations were no galling was observed experimentally, independent of the lubrication. For the configurations where galling is experimentally observed, the finite element model is able to predict it. The main drawback is that the prediction is always optimistic, the numerical drawing distance before galling being larger than the experimental one. This difference may be explained as a mesh effect. The numerical model predicts galling when a 0.2 mm element is fully damaged where the material affected by the galling onset is of some micrometers thickness [DON16]. Nevertheless, the proposed model is able to detect the strip rupture due to traction (S1-30%) or resulting from galling (strips of Set 2). The geometry of the fracture zone is in good agreement with experiments (Fig. 18). The numerical model is also able to take into account the influence of roughness since it predicts correctly the galling on only one side of the strip for the S2-10% configuration.

Table 7: Experimental vs numerical results of galling.

	set 1				set 2				
Results	16	20	25	30	7	9	10	12	15
Experiments									
Ls (mm)						9	220	32	15
galling on upper side	-	-	-	-	-	●	-	●	●
galling on lower side	-	-	-	-	-	●	●	●	●
strip rupture	-	-	-	●	-	●	●	●	●
Computations									
Ls (mm)						24	262	38	38
galling on upper side	-	-	-	-	-	●	-	●	●
galling on lower side	-	-	-	-	-	●	●	●	●
strip rupture	-	-	-	●	-	●	●	●	●
mean contact pressure (MPa)	275	280	280	280	225	300	225	260	250
mean friction Stress (MPa)	6.0	6.5	6.5	6	15	70	20	27	30

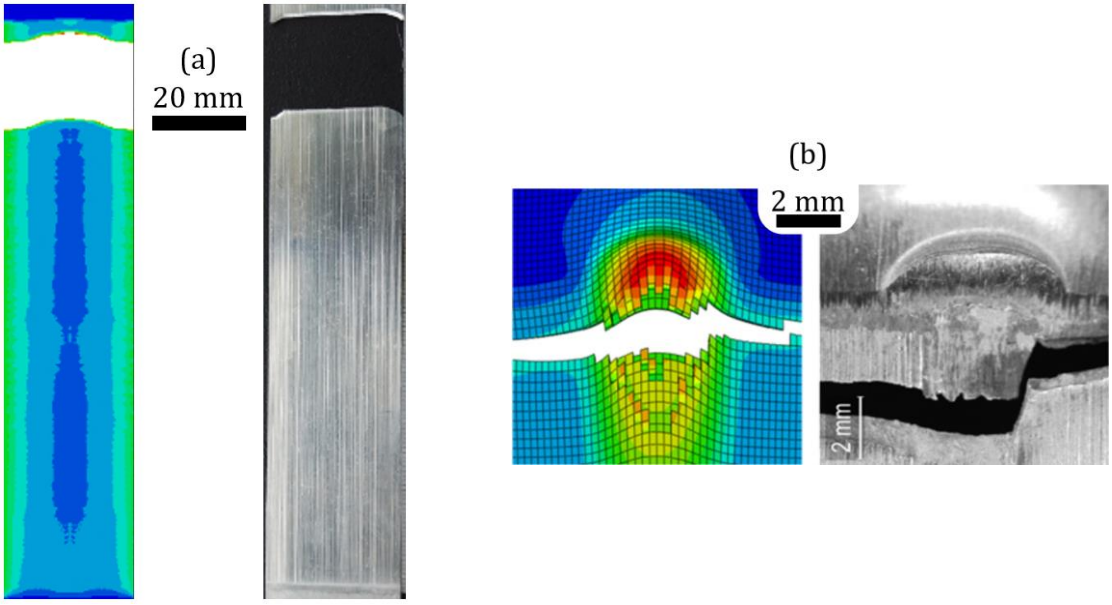

Figure 18: Numerical vs experimental geometry of the fractured strip. (a) configuration S1-30% without galling and a tensile fracture; (b) configuration S2-15% with galling and a zoom on the bulge area.

Conclusions

A methodology based on finite element computations is proposed to predict the galling onset of aluminium alloys in cold forming. The methodology assumes that galling starts as soon as one of the finite elements in the area of contact has reached a critical damage. The damage is calculated using Xue's model, which takes into account the effect of tangential stresses on the damage evolution. The tangential stress is calculated using Wilson's mixed lubrication model in order to explicitly take into account the roughness of the tools in the computation. Strip reduction tests were performed on aluminium AA6082 specimens, with and without lubricant. The following is concluded:

- The coefficient of adhesion needed to predict the tangential stress by Wilson's friction model needs to be identified only once for each lubrication configuration.
- The proposed numerical model is in good agreement with experiments. It is able to predict the onset of galling when galling actually occurs and it does not predict galling when no galling is experimentally observed.
- The model is sufficiently accurate to distinguish the effect of tool roughness.
- The computed sliding distance before galling occurs is always larger than the experimental one. This difference may be linked to the mesh size.
- The pick-up of strip material on the tool surface is not modelled. As soon as galling occurs, the damaged finite elements are deleted. This leads to a loss of material that has no physical meaning. Consequently the model is only valid until the onset of galling.

Acknowledgments

This work was conducted within the frameworks of the ELSAT2020 project supported by the French Ministry of Higher Education and Research, the French National Center for Scientific Research (CNRS), the Hauts de France Region and the Carnot Arts Institute. The work was also supported by the Danish Council for Independent Research [grant no. DFF – 4005-00130]. The authors gratefully acknowledge the support of these institutions.

References

[AND98] **J.L. Andreasen, N. Bay, L. De Chiffre**, Quantification of Galling in Sheet Metal Forming by Surface Topography Characterisation, *International Journal of Machine Tools & Manufacture* 38 (1998) 503-510.

[AST98] ASTM G98-17, Standard Test Method for Galling Resistance of Materials, *ASTM International*, West Conshohocken, PA, 2017, www.astm.org

[BAI07] **S. Bair**, *High Pressure Rheology for Quantitative Elastohydrodynamics*. Elsevier, 2007.

[BAI08] **Y. Bai, T. Wierzbicki,** A new model of metal plasticity and fracture with pressure and Lode dependence, *International Journal of Plasticity*, Vol. 24 (2008) 1071–1096

[BAY94] **N. Bay,** The state of the art in cold forging lubrication. *Journal of Materials Processing Technology,* Vol. 46 (1994) 19-40.

[BAY97] **N. Bay**, Cold forming of aluminium-state of the art, *Journal of Materials Processing Technology* 71 (1997) 76-90.

[BEL08] **A. Belotserkovets, A. Dubois, M. Dubar, L. Dubar, R. Deltombe, H. Vandekinderen, J.M. Damasse**, 2D asperity deformation of stainless steel strip in cold rolling, *International Journal of Material Forming*, Vol. 1 (2008) 351-354.

[BIL12] **E. Billur, T. Altan**, Challenges in forming advanced high strength steels. *Proceedings of New Developments in Sheet Metal Forming* (2012) 285-304.

[BLA99] **P. J. Blau, K. G. Budinski**, Development and use of ASTM standards for wear testing, *Wear,* Vol. 225–229 (1999) 1159–1170.

[BON05] **Bonora N, Gentile D, Pirondi A, Newaz G**. Ductile damage evolution under triaxial state of stress: theory and experiments. *International Journal of Plasticity*, Vol. 21 (2005) 981–1007.

[BOU15] **J. Bouquerel, B. Diawara, A. Dubois, M. Dubar, J.-B. Vogt, D. Najjar**, Investigations of the microstructural response to a cold forging process of the 6082-T6 alloy, *Materials & Design*, Vol. 68 (2015) 245-258.

[BRU18] **Brünig M, Gerke S, Schmidt M**. Damage and failure at negative stress triaxialities: experiments, modeling and numerical simulations. *International Journal of Plasticity* , Vol. 102 (2018) 70–82.

[BUD15] **K.G. Budinski, S.T. Budinski**, Interpretation of galling tests, *Wear*, Vol.332-333 (2015) 1185–1192.

[BUD97] **K. G. Budinski,** Guide to Friction, Wear, and Erosion Testing, ASTM International, ISBN 978-0-8031-4269-5.

[CAO13] **T.S. Cao**, Modeling ductile damage for complex loading paths, Doctoral dissertation, MINES ParisTech, 2013.

[CAO14] **T.-S. Cao**, Numerical simulation of 3D ductile cracks formation using recent improved Lode-dependent plasticity and damage models combined with remeshing, *International Journal of Solids and Structures*, Vol. 5-13 (2014) 2370-2381.

[CAO15] **T.S. Cao, C. Bobadilla, P. Montmitonnet, P.-O. Bouchard,** A comparative study of three ductile damage approaches for fracture prediction in cold forming processes, *Journal of Materials Processing Technology*, Vol. 216 (2015) 385–404.

[COR09] **O.N. Cora, M. Koc**, Experimental investigations on wear resistance characteristics of alternative die materials for stamping of advanced high-strength steels(AHSS), *International Journal of Machine Tools & Manufacture*, Vol. 49 (2009) 897–905.

[DAN06] **D. Daniel, G. Guiglionda, P. Litalien, R. Shahani**, Overview of forming and formability issues for high volume aluminum car body panels, *Materials Science Forum*, Vol. 519-521 (2006) 795-802.

[DEB16] **C. Debras**, Analyse multifactorielle de la dérive vers l'usure des outillages de frappe à froid (multifactorial analyses of tool wear onset in cold metal forming). Doctoral Dissertation, Université de Valenciennes et du Hainaut-Cambrésis, 2016 (in French).

[DEN19] **L. Deng, L. Pelcastre, J. Hardell, B. Prakash, M. Oldenburg**, Numerical investigation of galling in a press hardening experiment with AlSi-coated workpieces, *Engineering Failure Analysis*, Vol. 99 (2019) 85–96.

[DON16] **W. Dong, L. Xu, Q. Lin, Z. Wang**, Experimental and numerical investigation on galling behavior in sheet metal forming process. *International Journal of Advanced Manufacturing Technology*, Vol. 88 (2017) 1101-1109.

[DUB16] **A. Dubois**, Metal forming and lubrication, In: Saleem Hashmi (editor-in-chief). Reference *Module in Materials Science and Materials Engineering*, Elsevier, 1 (2016) 1-10.

[DUB17] **A. Dubois, O. Filali, C. Hubert, M. Dubar, L. Dubar, T.T. Pham**, Vers la caractérisation du collage des alliages d'aluminium en mise en forme à froid, in : *23ème Congrès Français de Mécanique*, Lille, 2017 (in French).

[DUB18] **A. Dubois, M. Dubar, C. Debras, K. Hermange, C. Nivot, C. Courtois**, New environmentally friendly coatings for hot forging tools, *Surface and Coatings Technology*, Vol. 344 (2018) 342-352.

[DUB96] **A. Dubois, J. Oudin, P. Picart**, Elastoplastic finite element analyses of an upsetting-sliding test for the determination of friction at medium and high contact pressure, *Tribology International*, Vol.29-7 (1996) 603-613.

[ECH11] **J. Echávarri Otero, P. Lafont Morgado, E. Chacón Tanarro, E. De La Guerra Ochoa, A, Díaz Lantada, J.M. Munoz-Guijosa, J.L. Muñoz Sanz**, Analytical model for predicting the friction coefficient in point contacts with thermal elastohydrodynamic lubrication. *Proceedings of the Institution of Mechanical Engineers, Part J: Journal of Engineering Tribology*, Vol 225 (2011) 181–191.

[ECH17] **J. Echávarri Otero, E. O. De La Guerra, E. Chacón Tanarro, B. Del Río López**, Friction coefficient in mixed lubrication: A simplified analytical approach for highly loaded non-conformal contacts. *Advances in Mechanical Engineering*, Vol. 9 (2017) DOI: 10.1177/1687814017706266.

[FIL18] **O. Filali, A. Dubois, L. Dubar, M. Dubar,** Towards the Numerical Prediction of Galling Onset in Cold Forming, *Key Engineering Materials*, Vol. 767 (2018) 103-110.

[GAO09] **X. Gao, T. Zhang, M. Hayden, C. Roe**, Effects of the stress state on plasticity and ductile failure of an aluminum 5083 alloy, International Journal of Plasticity, Vol. 25 (2009) 2366-2382.

[GOL93] **M. Gologanu, J.-B. Leblond, J. Devaux**, Approximate models for ductile metals containing non-spherical voids-case of axisymmetric prolate ellipsoidal cavities, *Journal of the Mechanics and Physics of Solids*, Vol. 41 (1993), pp. 1723-1754.

[GUE99] **J.D. Guerin, H. Bartys, A. Dubois, J. Oudin,** Finite element implementation of a generalized friction model: application to an upsetting-sliding test, *Finite Elements in Analysis and Design*, vol. 31 (1999) 193-207.

[GUR77] **A.L. Gurson**, Continuum theory of ductile rupture by void nucleation and growth: Part I-yield criteria and flow rules for porous ductile media, *Journal of Engineering Materials and Technology*, Vol. 99 (1977), pp. 2-15.

[HAN08] **M. Hanson, S. Hogmark, E. Coronel**, On adhesion of work material in metal forming, *Int. J. Microstructure and Materials Properties*, Vol. 3 (2008) 401-412.

[HAN09] **M. Hanson, S. Hogmark, S. Jacobson**, Influence from Tool Roughness on the Risk of Work Material Adhesion and Transfer, *Materials and Manufacturing Processes*, Vol. 24 (2009) 913–917.

[HAW16] **M. Hawryluk**, Review of selected methods of increasing the life of forging tools in hot die forging processes, *Archives of Civil and Mechanical Engineering*, Vol. 16 (2016) 845–866.

[HEI09] **J. Heinrichs, S. Jacobson**, Laboratory test simulation of galling in cold forming of aluminium, *Wear*, Vol. 267 (2009) 2278–2286.

[HEI10] **J. Heinrichs, S. Jacobson**, Laboratory test simulation of aluminium cold forming – influence from PVD tool coatings on the tendency to galling, *Surface & Coatings Technology*, Vol. 204 (2010) 3606–3613.

[HEI13] **J. Heinrichs, M. Olsson, S. Jacobson**, Influence of tool steel microstructure on initial material transfer in metal forming – In situ studies in the SEM, *Wear*, Vol. 302 (2013) 1249–1256.

[HUB11] **C. Hubert, L. Dubar, M. Dubar, A. Dubois, F. Lauro, D. Morin,** A non-associative flow rate formulation for Lemaitre's damage model. *in: 10th International Conference on Technology of Plasticity, ICTP 2011, Aachen, Germany* (2011) 889-894, ISBN: 9783514007840.

[HUM08] **S.R. Hummel**, Development of a galling resistance test method with a uniform stress distribution, *Tribology International*, Vol. 41 (2008) 175–180.

[JER15] **J. Jerina, M. Kalin**, Aluminium-alloy transfer to a CrN coating and a hot-work tool steel at room and elevated temperatures, *Wear*, Vol. 340-341 (2015) 82–89.

[KAR14] **P. Karlsson**, The influence of tool steel microstructure on galling, Doctoral dissertation, Department of Engineering and Physics, Karlstad University Studies, 2014.

[KIH90] **J. Kihara**, Tribological problems related with physical and chemical interaction among the tool, the workpiece and the lubricant, in: *Proceedings of Advanced Technology of Plasticity*, Vol. 4 (1990) 1693-1702.

[KIM07] **H. Kim, J. Sung, R. Sivakumar, T. Altan**, Evaluation of stamping lubricants using the deep drawing test, *International Journal of Machine Tools & Manufacture*, Vol. 47 (2007) 2120–2132.

[KLU16] **T. Klünsner, F. Zielbauer, S. Marsoner, M. Deller, M. Morstein, C. Mitterer**, Influence of surface topography on early stages on steel galling of coated WC-Co hard metals, *Int. Journal of Refractory Metals and Hard Materials*, Vol. 57 (2016) 24–30.

[KOR92] **D.A., Korzekwa, P.R. Dawson, W.R.D. Wilson**, Surface asperity deformation during sheet forming, *International journal of mechanical sciences*, Vol. 34.7 (1992) 521-539.

[LAU97] **F. Lauro, B. Bennani, P. Drazetic, J. Oudin, X. Ni,** Ductile damage and fracture finite element modelling of elasto-viscoplastic voided materials, *Computational Materials Science*, Vol. 7-3 (1997) 295-307.

[LAZ98] **L. Lazzarotto, L. Dubar, A. Dubois, P. Ravassard, J.P. Bricout, J. Oudin**, A selection methodology for lubricating oils in cold metal forming processes, *Wear*, Vol. 215 (1998) 1-9.

[LEM85] **Lemaitre J.** A continuous damage mechanics model for ductile fracture. *Journal of Engineering Materials and Technology*, Vol. 107 (1985) 83–89.

[LEM12] **Lemaitre J**. A course on damage mechanics. Springer Science & Business Media, 2012.

[MAL12] **R. Malhotra, L. Xue, T. Belytschko, J. Cao,** Mechanics of fracture in single point incremental forming, *Journal of Materials Processing Technology*, Vol. 212 (2012) 1573– 1590.

[MAL14] **Malcher L, Mamiya EN**. An improved damage evolution law based on continuum damage mechanics and its dependence on both stress triaxiality and the third invariant. *International Journal of Plasticity*, Vol. 56 (2014) 232–61.

[MER13] **M. Merklein, M. Johannes, M. Biasutti, M. Lechner**, Numerical optimisation of a shear specimen geometry according to ASTM. *Key Engineering Materials*, Vol. 549 (2013) 317-324.

[MOG17] **M. Moghadam, P. Christiansen, N. Bay**, Detection of the onset of galling in strip reduction testing using acoustic emission, *Procedia Engineering*, Vol. 183 (2017) 59 – 64.

[MOG20] **M. Moghadam, C.V. Nielsen, N. Bay,** Analysis of the risk of galling in sheet metal stamping dies with drawbeads. *Proceedings of the Institution of Mechanical Engineers, Part B: Journal of Engineering Manufacture*, Vol 234, No. 9 (2020) 1207–1214.

[NGU15] **Nguyen GD, Korsunsky AM, Belnoue JPH**. A nonlocal coupled damage-plasticity model for the analysis of ductile failure. *International Journal of Plasticity*, Vol. 65 (2015) 56–75.

[NIE18] **C.V. Nielsen, N. Bay**, Review of friction modeling in metal forming processes, *Journal of Materials Processing Technology*, Vol. 255 (2018) 234-241.

[OLS04] **D.D. Olsson, N. Bay, J.L. Andreasen**, Prediction of limits of lubrication in strip reduction testing, *CIRP Annals*, Vol. 53 (2004) 231-234.

[PAT78] **N. Patir, H.S. Cheng**, An average flow model for determining effects of three-dimensional roughness on partial hydrodynamic lubrication, *Journal of Lubrication Technology*, Vol. 100 (1978) 12-17.

[PHA15] **T.T. Pham**, Endommagement en surface des alliages d'aluminium en mise en forme à froid (*surface damage during the cold metal forming of aluminium alloys*), Doctoral dissertation, Université de Valenciennes et du Hainaut Cambrésis, 2015 (In French).

[POD17] **B. Podgornik, F. Kafexhiu, T. Kosec, J. Jerina, M. Kalin**, Friction and anti-galling properties of hexagonal boron nitride (h-BN) in aluminium forming, *Wear*, Vol. 388–389 (2017) 2–8.

[PUJ13] **J. Pujante, L. Pelcastre, M. Vilaseca, D. Casellas, B. Prakash**, Investigations into wear and galling mechanism of aluminium alloy-tool steel tribopair at different temperatures, *Wear*, Vol. 308 (2013) 193–198.

[PRU17] **C.I. Pruncu, T.T. Pham, A. Dubois, M. Dubar, L. Dubar**, Morphology of surface integrity as effect of cold forging of aluminum alloy, *Tribology Transactions*, Vol. 61-4 (2018) 632-639.

[ROD14] **M. Rodríguez-Millán, A. Vaz-Romero, A. Rusinek, J.A. Rodríguez-Martínez, A. Arias,** Experimental Study on the Perforation Process of 5754-H111 and 6082-T6 Aluminium Plates Subjected to Normal Impact by Conical, Hemispherical and Blunt Projectiles. *Experimental Mechanics*, Vol. 54 (2014) 729–742.

[SAA94] **Saanouni K, Forster C, Hatira FB.** On the anelastic flow with damage. *International Journal of Damage Mechanics*, Vol. 3 (1994) 140–69.

[SCH94] **E. Schedin**, Galling mechanisms in sheet forming operations, *Wear* 179 (1994) 123-128.

[SHE16] **H.R. Shercliff, M.F. Ashby**, Elastic Structures in Design, in: *Reference Module in Materials Science and Materials Engineering*, Elsevier (2016) 1-8.

[SIE14] **J.A. Siefert, S.S. Babu**, Experimental observations of wear in specimens tested to ASTM G98, *Wear*, Vol. 320 (2014) 111–119.

[SOE13] **T. Soejima, M. Yang,Z. Wang, Y. Yoshikawa**, Tribological Peculiarity of Galling Position in Square Cup Drawing, *Key Engineering Materials*, Vol. 535-536 (2013) 334-337.

[TRO17] **P. Tröber, H. A. Weiss, T. Kopp, R. Golle, W. Volk**, On the correlation between thermoelectricity and adhesive tool wear during blanking of aluminum sheets, *International Journal of Machine Tools & Manufacture*, Vol. 118–119 (2017) 91–97.

[TUR20] **Y. Türe, C. Türe**, An assessment of using Aluminum and Magnesium on CO2 emission in European passenger cars. *Journal of Cleaner Production,* Vol. 247 (2020) 119120.

[TVE84] **V. Tvergaard**, A. Needleman, Analysis of the cup-cone fracture in a round tensile bar, *Acta Metallurgica*, Vol. 32 (1984), pp. 157-169.

[UST17] **E. Üstünyagiz, C.V. Nielsen, P. Christiansen, P.A.F. Martins, N. Bay**, Continuous Strip Reduction Test Simulating Tribological Conditions in Ironing, *Procedia Engineering*, Vol. 207 (2017) 2286–2291.

[UST18] **E. Üstünyagiz, M.H. Sulaiman, P. Christiansen, C.V. Nielsen, N. Bay**, A Study on DLC Tool Coating for Deep Drawing, and Ironing of Stainless Steel, *Key Engineering Materials*, Vol. 767 (2018) 181-188

[UST19] **E. Üstünyagiz, C.V. Nielsen, P. Christiansen, P.A.F. Martins, T. Altan, N. Bay**, A combined numerical and experimental approach for determining the contact temperature in an industrial ironing operation, Journal Of Materials Processing Technology, Vol. 264 (2019) 249-258

[WAN14] **Z. Wang, M. Yang, Y. Yoshikawa** A Prediction Method for Galling Position in Square Cup Drawing, *Procedia Engineering*, Vol. 81 (2014) 1830 – 1835.

[WES16] **V. Westlund J. Heinrichs, M.Olsson, S. Jacobson**, Investigation of material transfer in sliding friction – topography or surface chemistry?, *Tribology International*, Vol. 100 (2016) 213–223.

[WIL88] **W.R.D. Wilson, S. Sheu,** Real area of contact and boundary friction in metal forming. *International*

[WIL90] **W.R.D Wilson**, Mixed lubrication in metal forming processes, in: *proceedings of Advanced Technology of Plasticity*, Vol. 4 (1990) 1667-1676.

[WIL91] **W.R.D. Wilson,** Friction Models for Metal Forming in the Boundary Lubrication Regime. *Journal of Engineering Materials and Technology*, Vol. 113 (1991) 60–68.

[WIL95] **W.R.D. Wilson, T.C. Hsu, X.B. Huang,** A Realistic Friction Model for Computer Simulation of Sheet Metal Forming Processes. *Journal of Engineering for Industry*, Vol 117 (1995) 202–209.

[WIL98] **W.R.D. Wilson, N. Marsault**, Partial Hydrodynamic Lubrication With Large Fractional Contact Areas. In: *Journal of Tribology,* Vol. 120 (1998), Nr. 1, S. 16–20.

[XUE07] **L. Xue**. *Ductile fracture modeling: theory, experimental investigation and numerical verification*. Doctoral dissertation, Massachusetts institute of technology, 2007.

[XUE09] **L. Xue**, Stress based fracture envelope for damage plastic solids, *Engineering Fracture Mechanics*, Vol. 76 (2009) 419–438.

[YAN08] **T.S. Yang,** Prediction of surface topography in lubricated sheet metal forming, *International Journal of Machine Tools & Manufacture*, Vol. 48 (2008) 768–777.

[YU19] **Yu F., Hendry MT, Li SX.** A stress triaxiality-dependent viscoplastic damage model to analyze ductile fracture under axisymmetric tensile loading. *Engineering Fracture Mechanics*, Vol. 211, (2019) 99-113.

[ZAB21] **A. Zabala, L. Galdos, C. Childs, I. Llavori, A. Aginagalde, J. Mendiguren, E. Saenz de Argandoña,** The Interaction between the Sheet/Tool Surface Texture and the Friction/Galling Behaviour on Aluminium Deep Drawing Operations. *Metals*, vol, 11 (2021) 979 doi.org/10.3390/met11060979

[ZEH19] **A. Zahedi, B. Mollaei Dariani, M. Javad Mirnia**, Experimental determination and numerical prediction of necking and fracture forming limit curves of laminated Al/Cu sheets using a damage plasticity model, *International Journal of Mechanical Sciences*, Vol. 153–154 (2019) 341–358.

Author contributions

Conceptualization	A. Dubois, L. Dubar
Methodology	A. Dubois, L. Dubar
Software	O. Filali
Validation	A. Dubois
Formal analysis	A. Dubois, O. Filali
Investigation	O. Filali, A. Dubois, M. Moghadam
Resources	A. Dubois, O. Filali
Data Curation	O. Filali
Writing - Original Draft	A. Dubois
Writing - Review & Editing	A. Dubois, L. Dubar,, C.V. Nielsen, M. Moghadam, O. Filali
Visualization (pictures and graphs)	O. Filali
Visualisation (drawing, pictures and graphs editing)	A. Dubois
Supervision	A. Dubois, L. Dubar
Project administration	A. Dubois, L. Dubar
Funding acquisition	A. Dubois, L. Dubar, C.V. Nielsen